**Supporting Information**

# Cover matters: Enhanced performance of multistage solar evaporator with tuned optical and thermal cover properties

Shiteng Li[a,b,c,d†], Shang Liu[a,b†], Qijun Yang[a,b], Shuai Deng[c,d], Meng Lin[a,b*]

[a]*Shenzhen Key Laboratory of Intelligent Robotics and Flexible Manufacturing Systems, Department of Mechanical and Energy, Southern University of Science and Technology, Shenzhen 518055, China.*

[b]*SUSTech Energy Institute for Carbon Neutrality, Southern University of Science and Technology, Shenzhen 518055, China.*

[c]*National Industry-Education Platform for Energy Storage (Tianjin University), Tianjin 300350, China*

[d]*Skate Key Laboratory of Engines, Tianjin University, Tianjin 300350, China*

[†]These authors contributed equally to this work.

*To whom correspondence should be addressed: linm@sustech.edu.cn

## Section S1 – Model development

### 1.1 Absorber temperature ($T_{abs}$) model

The lumped parameter model of the absorber with different cover designs was built. A detailed comparative analysis of the effect of cover properties, i.e., optical transmission, thermal conductivity, and thickness, on optical and heat losses was performed. Based on this analysis, design and operation guidance are provided for the device's performance optimization. For simplicity, we made the following assumptions during the modeling process: *i)* The device operates in a steady state; *ii)* the side wall heat loss accounts for a small proportion of the total heat loss and hence can be neglected; *iii)* at the bottom of the absorber, a well-insulated layer was considered, and hence the bottom heat loss can be omitted, and *iv)* the temperature difference between the sky and the ambient is neglected.

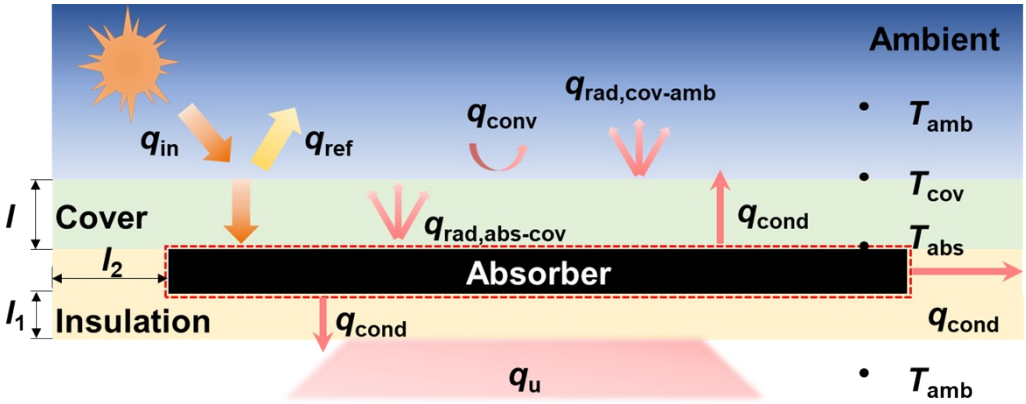


**Figure S1. Schematic of the model system.**

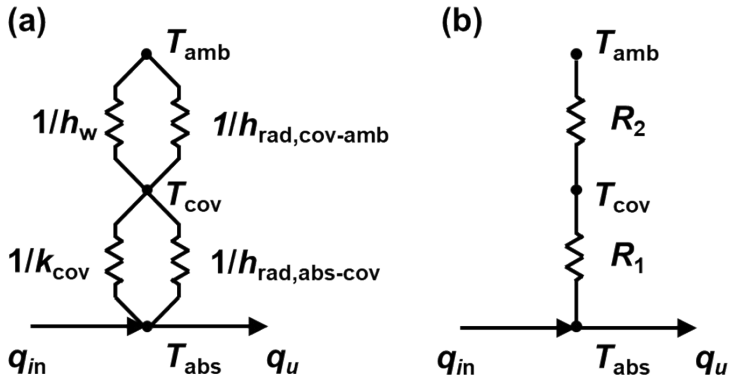


**Figure S2. Thermal network diagram of the solar absorber with a cover: (a) in**

**terms of conduction, convection, and radiation resistances; (b) in terms of thermal resistances between two surfaces.**

The size of the cover in the device is 30 × 30 × 10 $mm^3$, the absorber size is 25 × 25 × 1 $mm^3$, and the side and bottom of the absorber are coated with insulation materials with low thermal conductivity. Affected by the transmittance $\tau$ of the cover and the absorptance $\alpha$ of the absorber, there is an optical loss when the sunlight shines on the surface of the absorber. When the sunlight reaches the surface of the absorber, it will undergo photothermal conversion, part of which will be converted into useful energy that the absorber can output, and part of which will be converted into heat loss. The total heat loss of the absorber includes top heat loss, side heat loss, and bottom heat loss. We first introduce the top heat loss of the absorber.

The energy absorbed by sunlight passing through the cover to the absorber surface is expressed as

$$S = \tau\alpha q_{\text{sun}} \tag{S1}$$

where $\tau$ is the transmittance of the cover, $\alpha$ is the absorption of the absorber. The energy that can be utilized is expressed as

$$q_{\text{u}} = \left[ S - U_{\text{L}} \left( T_{\text{abs}} - T_{\text{amb}} \right) \right] \tag{S2}$$

where $T_{\text{abs}}$ and $T_{\text{amb}}$ are the absorber temperature and ambient temperature, respectively, $U_{\text{L}}$ is the total heat loss coefficient, it includes top heat loss coefficient $U_{\text{t}}$, side heat loss coefficient $U_{\text{e,}}$ and bottom heat loss coefficient $U_{\text{b}}$ :

$$U_{\text{L}} = U_{\text{t}} + U_{\text{e}} + U_{\text{b}} \tag{S3}$$

The top heat loss coefficient $U_{\text{L}}$ was first calculated. There are heat conduction and radiation heat transfer between the absorber and the cover, equivalent thermal resistance is shown in Figure S2. The conductivity and radiation thermal resistance are $l/k_{\text{cov}}$ and $1/h_{\text{rad,abs-cov}}$, respectively. The thermal resistant $R_1$ is expressed as

$$R_{\text{l}} = \frac{l}{k_{\text{cov}} + l h_{\text{rad,abs-cov}}} \tag{S4}$$

where $l$ is the thickness of the cover, $k_{cov}$ is the thermal conductivity of the cover, $h_{rad,abs-cov}$ is the radiation heat transfer coefficient from absorber to cover, it can be expressed as

$$h_{rad,abs-cov} = \frac{\sigma\left(T_{cov}^2 + T_{abs}^2\right)\left(T_{cov} + T_{abs}\right)}{\frac{1-\varepsilon_{abs}}{\varepsilon_{abs}} + \frac{1}{F} + \frac{\left(1-\varepsilon_{cov)}\right)A_{abs}}{\varepsilon_{cov}A_{cov}}} \tag{S5}$$

where $\sigma$ = 5.67 × $10^{-8}$ W $m^{-2}$ $K^{-4}$ is the Stefan-Boltzmann constant, $T_{cov}$ is the temperature on the surface of the cover, $\varepsilon_{abs}$ is the emissivity of the absorber, $F$ is the angle coefficient, taking an approximate value of 1, $A_{abs}$ and $A_{cov}$ represent the areas of the absorber and cover, respectively.

The heat transfer between the cover and the ambient includes natural convection heat transfer on the upper surface of the cover and radiation heat transfer of the cover to the ambient. Their equivalent thermal resistance is also shown in Figure S2. The convection and radiation thermal resistance are $1/h_w$ and $1/h_{rad,cov-amb}$, respectively. The thermal resistance $R_2$ is expressed as

$$R_2 = \frac{1}{h_w + h_{rad,cov-amb}} \tag{S6}$$

where $h_w$ is the natural convection heat transfer coefficient, $h_{rad,cov-amb}$ is the radiation heat transfer coefficient from cover to ambient, they can be represented separately as

$$h_w = 2.8 + 3.0v \tag{S7}$$

$$h_{rad,cov-amb} = \frac{\varepsilon_{cov}\sigma\left(T_{cov}^4 - T_{amb}^4\right)}{T_{cov} - T_{amb}} \tag{S8}$$

where $v$ is the natural wind speed, $\varepsilon_{cov}$ is the emissivity of the cover, and $T_{amb}$ is the temperature of ambient. The total thermal resistance from the absorber to the ambient is equal to ($R_1$+$R_2$), we can use the top heat loss coefficient $U_t$ to calculate the top heat loss $q_{loss,t}$ will be simpler

$$q_{loss,t} = \frac{T_{abs} - T_{amb}}{R_1 + R_2} = U_t\left(T_{abs} - T_{amb}\right) \tag{S9}$$

$$U_{\mathrm{t}}=\frac{1}{R_1+R_2}=\left(\frac{l}{k_{\mathrm{aero}}+lh_{\mathrm{rad,abs\text{-}aero}}}+\frac{1}{h_{\mathrm{w}}+h_{\mathrm{rad,aero\text{-}amb}}}\right)^{-1} \tag{S10}$$

The heat loss coefficient on the side $U_{\mathrm{e}}$ of the absorber can be approximately estimated as

$$U_{\mathrm{e}}=\left(\frac{k_{\mathrm{e}}}{l_2}\right)\left(\frac{A_{\mathrm{e}}}{A_{\mathrm{abs}}}\right) \tag{S11}$$

where $k_{\mathrm{e}}$ and $l_2$ are the thermal conductivity and thickness of insulation materials on the side, respectively, $\frac{A_{\mathrm{e}}}{A_{\mathrm{abs}}}$ is the ratio of the side area to the front area of the absorber. The side area of the absorber is much smaller than the front wall area, and the heat leaked from the side can be ignored. The absorber bottom is insulated with silica aerogel with very low thermal conductivity (~0.02 W $m^{-1}$ $K^{-1}$), with only minimal heat conduction loss.

The absorber efficiency can be expressed by

$$\eta_{\mathrm{abs}}=\tau\alpha-\frac{U_L\left(T_{\mathrm{abs}}-T_{\mathrm{amb}}\right)}{q_{\mathrm{sun}}} \tag{S12}$$

Under the device operation stable, the energy transferred from the absorber to the cover is equivalent to the energy transmitted from the cover to the surrounding ambient. Additionally, this energy exchange is also commensurate with the top heat loss coefficient $U_{\mathrm{t}}$ from the absorber to the ambient. Therefore, the temperature at the surface of the cover and the absorber adhere to

$$T_{\mathrm{cov}}'=T_{\mathrm{abs}}-\frac{U_{\mathrm{t}}\left(T_{\mathrm{abs}}-T_{\mathrm{amb}}\right)}{\frac{k_{\mathrm{cov}}}{l}+h_{\mathrm{rad,abs-cov}}} \tag{S13}$$

The cover surface temperature $T_{\mathrm{cov}}'$, can only be calculated when the top heat loss coefficient $U_{\mathrm{t}}$ is known. Therefore, an iterative process is required when computing $U_{\mathrm{t}}$. $U_{\mathrm{t}}$ depends on the unknown quantity $T_{\mathrm{cov}}$, we need to assume a cover surface temperature $T_{\mathrm{cov}}$ for calculation. We then iterate until $T_{\mathrm{cov}}$ converges (i.e. $|T_{\mathrm{cov}}-T_{\mathrm{cov}}'|<$ 0.01 K, where 0.01 K is the tolerance used in this work). Figure S3a shows the calculation flow of the absorber temperature model.

### 1.2 Multistage solar evaporator (MSE) device model

Coupling the absorber stagnation temperature model with the Multistage solar evaporator device model, the $T_{abs}$ also become an unknown parameter. It is assumed that all the energy of the absorber can be used for evaporation, i.e., the energy of the first stage, $q_{evap,1}$ can be expressed as:

$$q_{evap,1} = q_u \tag{S14}$$

Simultaneously, the heat carried by per stage vaporization $q_{evap,n}$ is related to the vapor flux $J_{evap,n}$ through the latent heat $h_{fg}$ and molecular weight of water $M$,

$$q_{evap,n} = Mh_{fg,n}J_{evap,n} \tag{S15}$$

where $h_{fg,n} = h_{fg,n}(T_{evap})$ are evaporation temperature dependent, at lower vapor fluxes, vapor transport depends on diffusion and is governed by Fick's law,

$$J_{evap,n} = D_a \frac{c_{evap,n} - c_{cond,n}}{b} \tag{S16}$$

where $c_{evap} = c_{evap}(T_{evap})$ and $c_{cond} = c_{cond}(T_{cond})$ are temperature dependent, $b$ is the thickness of the evaporation layer, according to the assumption,

$$T_{cond,n-1} = T_{evap,n} \tag{S17}$$

$$T_{cond,n} = T_{cool} \tag{S18}$$

Figure S3b shows the computational flow of the coupled heat and mass transfer model. Different combinations of absorber and cover temperatures are assumed for the calculation, and the heat and mass transfer calculation process is completed when the $|T_{cov} - T_{cov}'| < 0.01$ K and the $|T_{evap,1} - T_{abs}| < 0.01$ K. The heat and mass transfer calculation process is completed by the coupled heat and mass transfer model. The energy balance relationship of the overall system can be expressed as,

$$q = q_{sun} = q_{loss,opt} + q_{loss,t} + q_u \tag{S19}$$

The optical loss $q_{loss,opt}$ due to the transmittance of the cover and absorptance of the absorber is given by

$$q_{loss,opt} = (1-\tau)(1-\alpha)q_{sun} \tag{S20}$$

The top heat loss of the cover from two aspects

$$q_{\text{loss,t}} = q_{\text{conv,cov-amb}} + q_{\text{rad,cov-amb}} \tag{S21}$$

The convection heat loss on the cover is expressed as

$$q_{\text{conv,cov-amb}} = h_{\text{w}} \left( T_{\text{cov}} - T_{\text{amb}} \right) \tag{S22}$$

The radiation heat loss from the cover is given by

$$q_{\text{rad,cov-amb}} = \varepsilon_{\text{cov}} \sigma \left( T_{\text{cov}}^4 - T_{\text{amb}}^4 \right) \tag{S23}$$

The evaporation rate can be calculated by

$$r_{\text{evap,sim}} = 3.6 M J_{\text{evap}} \tag{S24}$$

where coefficient 3.6 is the result of converting units of "g" and units of "s", $M$ is the molecular weight of water, and $J_{\text{evap}}$ is the vapor flux, where $J_{\text{evap}} = J_{\text{evap,1}} + J_{\text{evap,2}} + \ldots J_{\text{evap,n}}$.

Finally, the evaporation efficiency also needs to be calculated

$$\eta_{\text{evap,sim}} = \frac{q_{\text{evap}}}{q_{\text{sun}}} \tag{S25}$$

where $q_{\text{evap}} = q_{\text{evap,1}} + q_{\text{evap,2}} + \ldots + q_{\text{evap,n}}$.

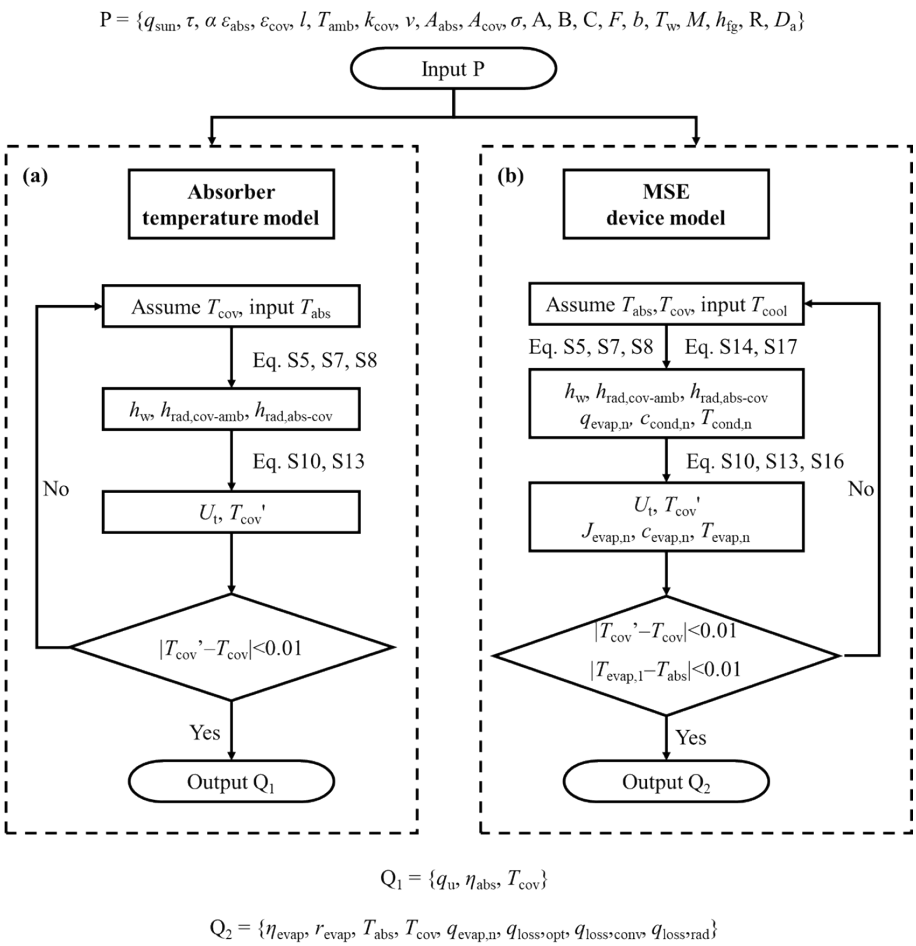


Figure S3. The corresponding iterative algorithm is used to evaluate the heat and mass transfer of (a) the absorber, and (b) the MSE device.

**Section S2 – Effect of absorber temperature ($T_{abs}$)**

HBP-PTFE loses its hydrophobic properties when the $T_{abs}$ are too high (see Figures S22 and S23 for details). The range of values of transmittance and thermal conductivity for commonly used glass, acrylic, and aerogel are given, and the specific values are shown in Table S1. In the calculations, it was found that there was an overheating zone in the MSE device of aerogel covered at $n$ = 10 and 3 suns (Figure S4c).

**Table S1. Summary of commonly used ranges of values for transmittance and thermal conductivity of glass, acrylic, and aerogel.**

| Material type | Transmittance (%) | Thermal conductivity ($W\ m^{-1}\ K^{-1}$) | Ref |
|---|---|---|---|
| Glass | 91.74 | - | 1 |
| | 84 - 96 | - | 2 |
| | 90 | 1 | 3 |
| | 90 | 0.76 | 4 |
| | 95 | 0.19 | 5 |
| | 86 - 92 | 0.19 - 0.21 | 6 |
| Acrylic | - | 0.5 | 7 |
| | 95 | 0.02 | 8 |
| | 88 | 0.011 | 9 |
| Aerogel | 76 - 88 | 0.1-0.19 | 10 |
| | 71 - 77 | 0.0215 - 0.0255 | 11 |
| | 90 | 0.02 | 12 |
| | - | 0.013 | 13 - 15 |

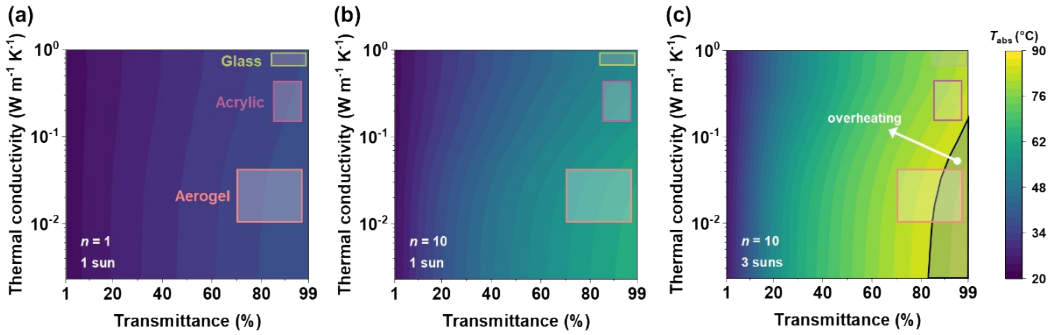


**Figure S4. The $T_{abs}$ as a function for transmittance and thermal conductivity at (a) $n$ = 1, 1 sun. (b) $n$ = 10, 1 sun. (c) $n$ = 10, 3 suns.**

**Section S3 – Energy breakdown analysis**

Equations S19 - S21 give the calculation of the energy balance. The breakdown of the total $q_{sun}$, using the first stage evaporator of the MSE device as the destination of the $q_u$ in the absorber, allows the energy distribution to be analyzed visually.

Using the transmittance and thermal conductivity of glass, acrylic, and aerogel in Table S2 as reference values for calculations, the reasons for the differences in gain due to the different cover materials of the MSE devices were analyzed through energy breakdown. Figure S7a shows the energy breakdown at different stages $n$ and solar irradiation for different cover conditions. At lower solar irradiation and a smaller number of stages, e.g. 1 sun, $n$ = 1, the $T_{abs}$ is low and the difference can be ignored (see Figure S5b), the heat loss due to heat conduction varies is little between cover conditions, so the energy available for evaporation has only a small difference. As the number of evaporation stages increases, i.e., 1 sun, $n$ = 10, the $T_{abs}$ gradually increase. At this time, the difference in thermal conductivity makes the temperature difference between the covers larger (see Figure S5c). Thus the difference in heat loss increases, and the very low thermal conductivity of the aerogel shows a great advantage. However increasing the solar irradiation, the difference in energy available for evaporation decreases instead. At this point, the $T_{abs}$ increase (Figure S5b), and the $T_{cov}$ difference rises further (Figure S5c). However, according to Eqs. S22 and S23, the convection and radiation heat transfer losses are determined by the temperature difference between the cover and the ambient, which is smaller than the multiplier of the increase in solar irradiation, so the heat loss gap narrows.

The increase in evaporation efficiency ($\eta_{evap}$) with the number of stages ($n$) is not linear because of heat losses. Based on the assumption that each successive stage utilizes 82.5% of the energy, we identified that a 10-stage device strikes the best balance between maximizing efficiency and minimizing device complexity (see Figure S6). Furthermore, the thickness of the evaporation layer in the MSE device was kept constant at 0.71 mm for all cases. The predicted effect of varying the evaporation layer thickness on the $\eta_{evap}$ is presented in Figure S7 (the thicker the evaporation layer, the

lower the energy reuse rate).

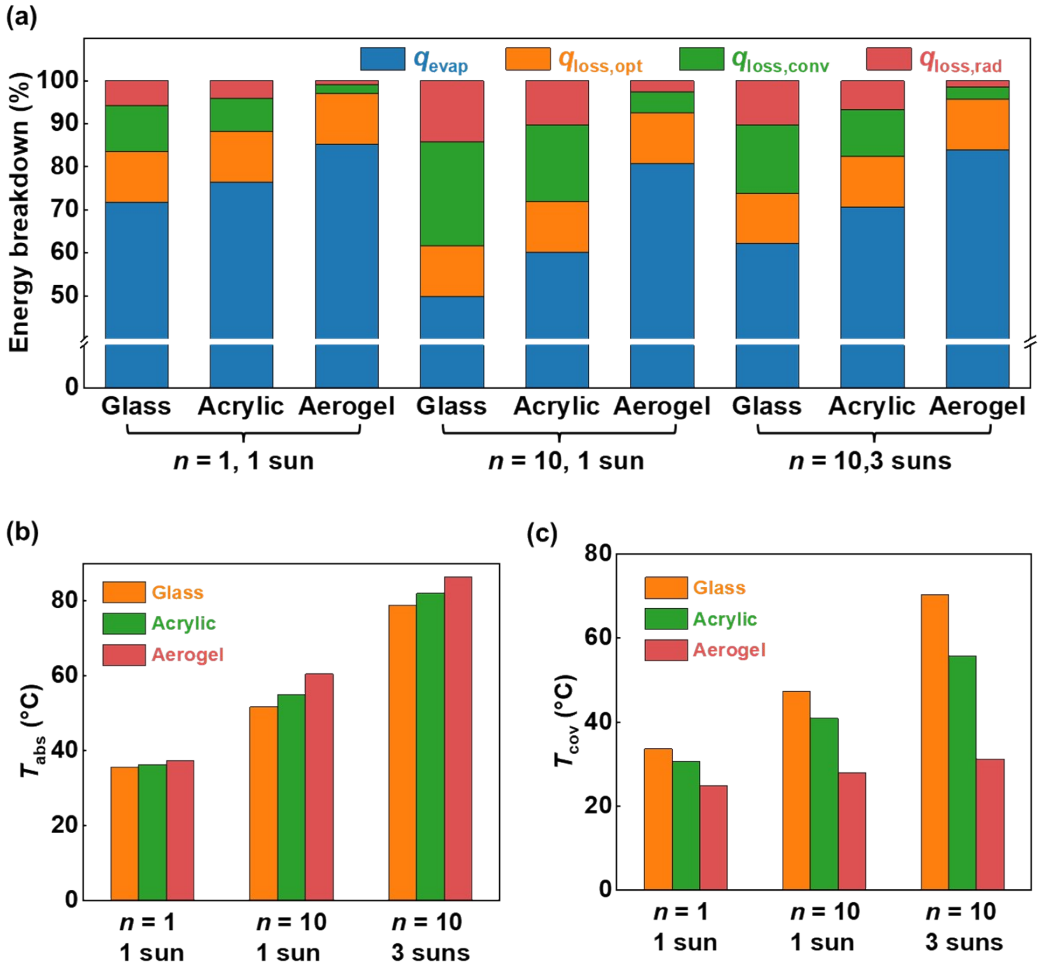


**Figure S5. (a) Energy breakdown, (b) $T_{abs}$, and (c) $T_{cov}$ for different types of cover materials case at $n$ = 1, 1 sun; $n$ = 10, 1 sun; $n$ = 10, 3 suns. The values of transmittance and thermal conductivity of the glass, acrylic, and aerogel are given in Table S2.**

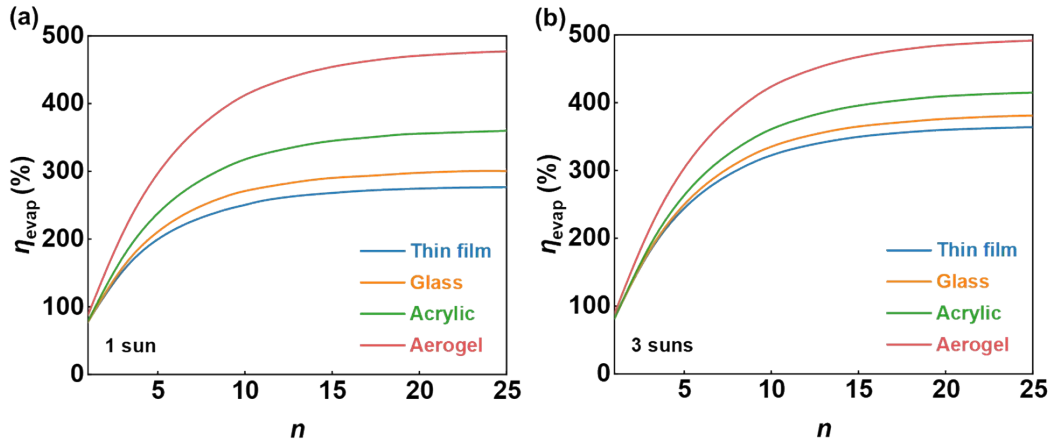


**Figure S6. The evaporation efficiency ($\eta_{evap}$) obtained through simulation in this work predicted with different stages. (a) 1 sun. (b) 3 suns.**

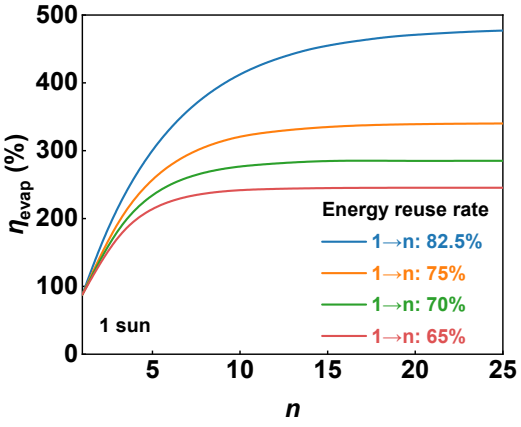


**Figure S7. Prediction of $\eta_{evap}$ for MSE device with different stages under 1 sun. The differences of energy reuse rates for the following stages were caused by the change of the thickness of the evaporation layer.**

**Table S2. The transmittance and thermal conductivity values are taken for the Figure S5 case.**

| Cover type | Transmittance | Thermal conductivity |
|---|---|---|
| Glass | 90% | 0.9 W $m^{-1}$ $K^{-1}$ |
| Acrylic | 90% | 0.2 W $m^{-1}$ $K^{-1}$ |
| Aerogel | 90% | 0.023 W $m^{-1}$ $K^{-1}$ |

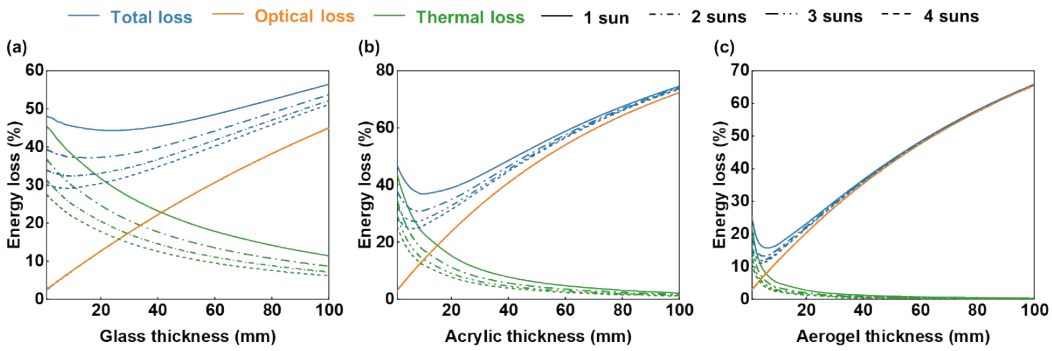


**Figure S8. (a) The energy loss as a function of (a) glass, (b) acrylic, and (c) aerogel thickness at different solar irradiations.**

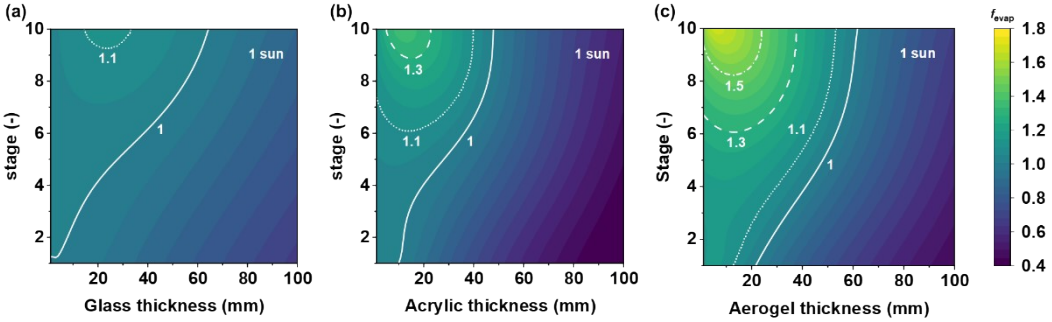


**Figure S9. The $f_{evap}$ as a function of (a) glass, (b) acrylic, (c) aerogel thickness and stage at MSE device (1 sun).**

## Section S4 – Preparation and characterization of cover materials

### 4.1 Materials

Tetramethoxysilane (Aladding, 98.0%), Ammonia solution (Aladding, AR, 25 - 28%), Methanol (Aladding, AR, 99.5%), Chlorotrimethylsilane (Aladding, GC, > 98.0%), Deionized water (Prepared in the laboratory), Ethanol (Aladding, AR, 95.0%)

### 4.2 Preparation

The transparent silica aerogel was synthesized using a one-step sol-gel method. Tetramethoxysilane (TMOS) as a silicon source and ammonia solution as a catalyst were diluted with methanol, and then the two solutions were mixed and stirred. The molar ratio of each chemical was $NH_3$:TMOS:water:methanol = 0.0057:1:3:7.09. Pour the stirred solution into the prepared mold to complete the gel process. Subsequently, the sample was placed within a container filled with ethanol for solvent replacement, a process repeated 3 - 5 times and spanning approximately one week. Take out the sample and immerse it in an ethanol solution containing Chlorotrimethylsilane (1:9 volume ratio of Chlorotrimethylsilane in ethanol) for surface hydrophobic modification. After approximately 24 hours, remove any excess hydrophobic reagents from the surface with ethanol. Throughout the process of supercritical drying, ethanol was delicately dispensed onto the surface of the wet gel to maintain its moisture content. To minimize the risk of sample cracking, the gradual increase in temperature and pressure was executed meticulously, thus minimizing the stress on the sample during the drying phase. Following the drying process, it was advisable to gradually decrease the pressure within the supercritical dryer chamber from 9.5 MPa to ambient levels, employing a controlled exhaust flow rate. To enhance the transmittance of the aerogel, it was imperative to subject the dried sample to annealing at 200 °C for 24 hours.

### 4.3 Characterization

The hydrophobic properties of aerogel are characterized by a water contact angle test (Figure S10a). The porous structure of the aerogel without additional hydrophobic treatment step collapses upon exposure to water, which affects the optical transmittance property of the aerogel, as shown in Figure S10b. The hydrophobized aerogel showed excellent hydrophobicity, with a surface water contact angle of about 140°, and remained intact after exposure to water.

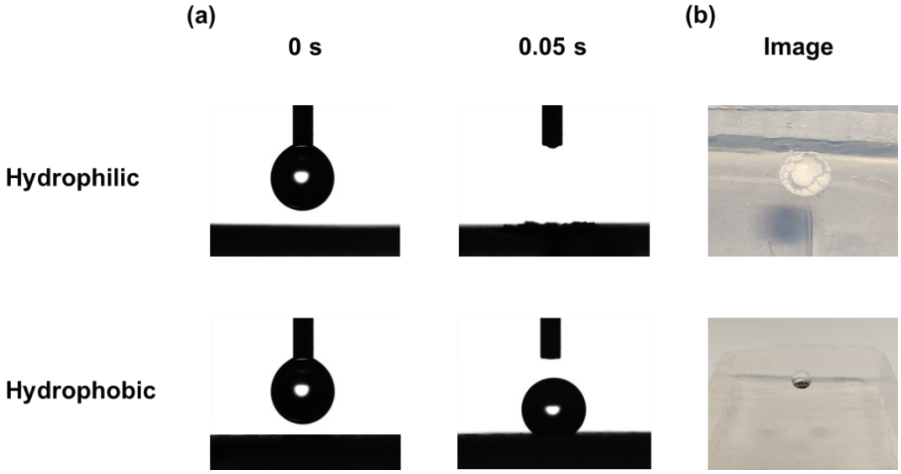


**Figure S10. Hydrophilic and hydrophobic properties of aerogels. (a) Contact angle picture of hydrophilic and hydrophobic aerogels by dripping water after 0 s and 0.05 s. (b) Images of hydrophilic and hydrophobic aerogels after dripping water.**


**Figure S11. Images of (a) glass, (b) acrylic, and (c) aerogel samples (10 mm thick) on a piece of paper with the SOUTHERN UNIVERSITY OF SCIENCE AND TECHNOLOGY logo.**

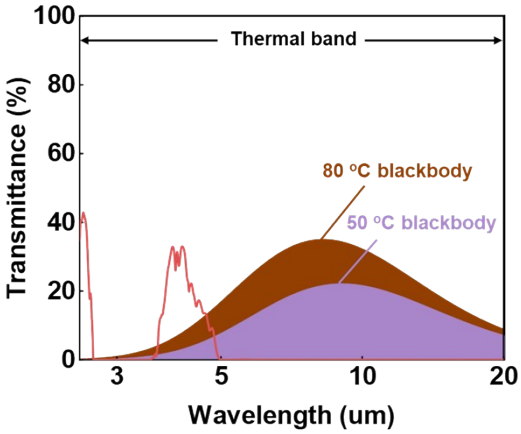


**Figure S12. Transmittance spectrum of the aerogel in the thermal band.**

## Section S5 – Supplemental experimental procedure

### 5.1 Absorber preparation and characterization

The hydrophobic porous polytetrafluoro-ethylene (HBP-PTFE) membrane with a pore size of 0.1 μm was obtained from the Haining Chuangwei Filter Equipment Factory. The nanocarbon powder was purchased from Shanghai Aladdin Biochemical Technology Co., Ltd. The ethanol (ACS, 99.5%) was obtained from Shanghai Aladdin Biochemical Technology Co., Ltd.

The HBP-PTFE membrane with 0.1 μm pore size was cut into 2.5 × 2.5 $cm^2$. The nanocarbon powder was uniformly dispersed in ethanol, and nafion solution was also added to enhance the adhesion of the nanocarbon powder. The homogeneous suspension was sprayed on the back of the HBP-PTFE membrane with a spray gun under the external environment of 50 °C, and the absorbing layer was obtained by drying in a drying cabinet for 1h. The absorptance of the absorber layer in the range of 0.25 to 2.5 μm is shown in Figure S13.

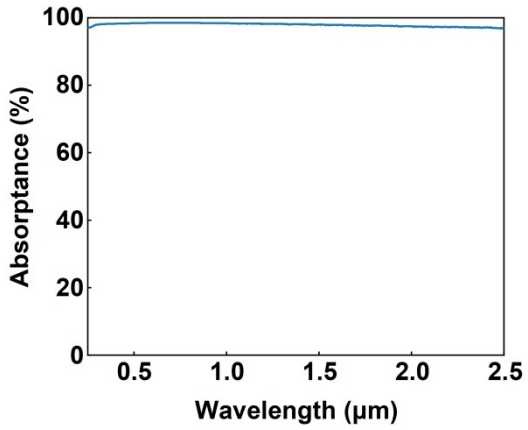


**Figure S13. Absorptance spectra of the absorber in the solar band.**

### 5.2 Absorber stagnation temperature measurement

The stagnation temperature is the maximum temperature the absorber can reach when

exposed to solar radiation under no-flow conditions, at which point all absorbed solar energy is released to the environment as heat losses rather than being converted into useful thermal energy[8]. The diagram of the system for measuring stagnation temperature is shown in Figure S14, including a solar simulator, a photoradiometer, a thermocouple, a data collector and a computer, and an insulated absorber. The stagnation temperature was tested under 1 sun irradiation (ambient temperature: 23 $^{o}$C; humidity: 60%). The incident intensity was provided by a solar simulator, and the solar power meter was used to calibrate before testing. A nanocarbon-based absorber (2.5 × 2.5 cm$^2$, and the solar-weighted absorptance ≈ 98%, details see Figure S13) was used to capture the solar irradiation. Three materials (glass, acrylic, and aerogel) 3 × 3 × 1 cm$^3$ in size were directly placed on top of the absorber as the cover. An aluminum aperture was used to reflect solar radiation away from the inactive areas of the absorber. To minimize heat losses, the bottom of the absorber was insulated with ultra-low thermal conductivity silica aerogel (8 × 8 × 4 cm$^3$). Two K-type thermocouples were positioned at the center of the absorber and on top of the cover, respectively (see Figure S15b). Temperature measurements were initiated upon switching on the solar simulator. As shown in Figure S15, two modes of operation were tested for comparison purpose: uncovered (Figure S15a) and covered (Figure S15b), and the only difference between the devices was the presence or absence of a cover on top of the absorber.

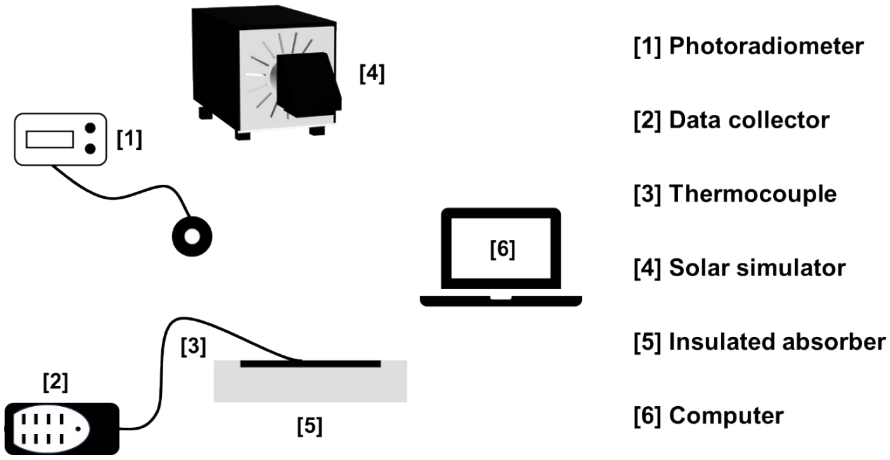


**Figure S14. The stagnation temperature test schematic.**

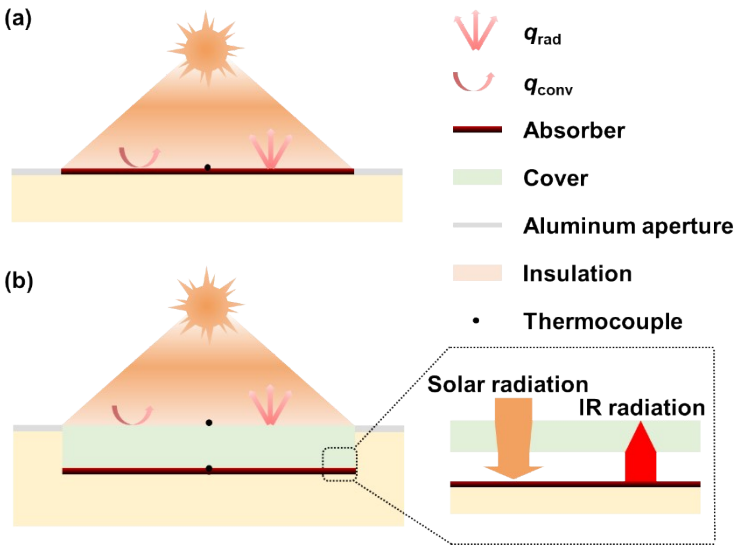


**Figure S15. Schematic diagram of the absorber stagnation temperature measurement device.**

### 5.3 Multistage solar evaporator (MSE) device

Figure S16 illustrates the two modes of operation of the MSE device with a cover design and an uncovered design. The only difference between the two designs is the covering on top of the absorber layer. The top of the absorber in Figure S16a is transmittance materials, i.e. glass, acrylic, and aerogel, however, in Figure S16b is a very thin polyethylene (PE) resin film, called the thin film case. They both have the same effect of changing the direction of vapor transport. To verify that the thin film does not produce the same effect to the cover, we used the model to compare the two working conditions of uncovered and top covered with a thin film at $n$ = 10 under 1 sun, and the results are shown in Figure S17. The absorber layer uses the HBP-PTFE membrane loaded with nanocarbon powder as mentioned in Section S5.1. Regenerated cell fibers purchased from Anhui Hening Daily Necessities Co., Ltd. with a thickness of 0.71 mm and a thermal conductivity of 0.71 W $m^{-1}$ $K^{-1}$ as evaporation layer (2.5 × 2.5 $cm^2$), condensation layer (2.5 × 2.5 $cm^2$), and water transport channel (10 × 1 $cm^2$), respectively.

The water contact angle and SEM picture of regenerated cell fibers are shown in Figure S18c and Figure S18d, respectively. Long strip regenerated cell fibers are inserted into the evaporation layer and condensation layer as seawater inlet and fresh water outlet, respectively. The HBP-PTFE membrane was placed between the evaporation layer and the condensation layer to separate seawater and fresh water. HBP-PTFE membrane purchased from Haining Chuangwei Filter Equipment Factory with a thickness of 0.18 mm and a thermal conductivity of 0.13 W $m^{-1}$ $K^{-1}$. HBP-PTFE membrane smaller pore size is not conducive to vapor transmission, while too large pore size will reduce the separation effect of seawater and vapor, we chose the HBP-PTFE membrane with a pore size of 1 μm as the PTFE layer, and its water contact angle and SEM test results are shown in Figure S18a and Figure S18b. It is worth mentioning that the pore size of the PTFE layer membrane is larger than that of the absorber layer, which makes the vapors more inclined to be transported downward, in addition, the smaller pore size of the HPB-PTFE membrane in the absorber layer will be more effective in preventing seawater from diffusing to the top of the absorber, so that salt deposition does not occur on the top of the absorber. The PE resin purchased from AsahiKASEI (China) Investment Limited was used as the sealing layer with a thickness of 0.01 mm and a thermal conductivity of 0.07 W $m^{-1}$ $K^{-1}$. The sealing layer can prevent the fresh water in the condensation layer from being contaminated by the seawater in the next stage evaporation layer. The components of a single stage of the MSE device are described above, and repeating the process will result in a multistage device. However, each subsequent stage does not require an additional absorber layer, and the heat required for their evaporation comes from the latent heat of condensation of the previous stage. We added a cooling layer at the end stage to enhance the condensation effect, using regenerated cell fibers (5 × 5 $cm^2$) with a large area. Long strips of regenerated cell fibers (15 × 3 $cm^2$) are inserted on both sides of the cooling layer as the inlet and outlet of the cooling water, respectively. The difference in height between the two is kept at a certain level to form a siphon effect to realize the passive work.

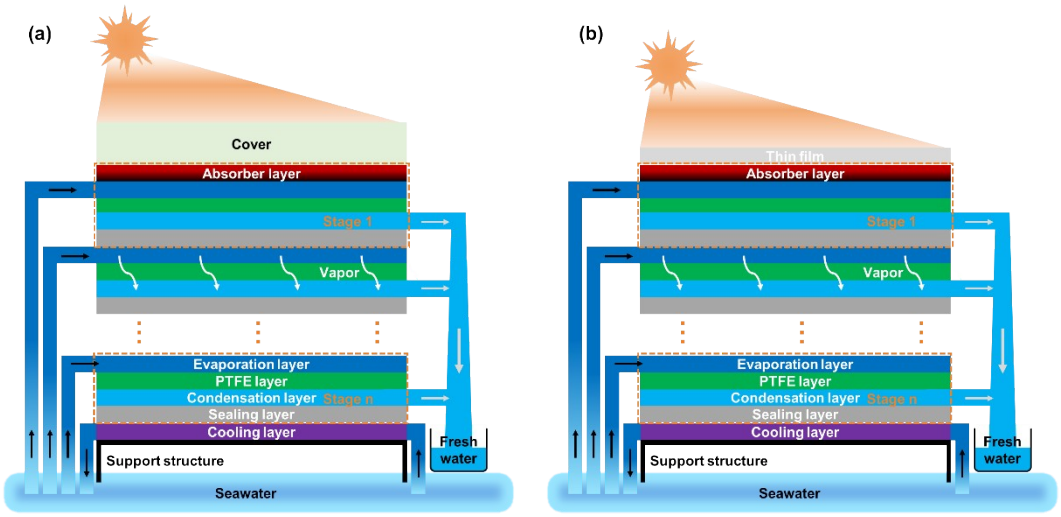


**Figure S16. Schematic diagram of the MSE device with (a) glass, acrylic, and aerogel as cover mode and (b) thin film mode.**

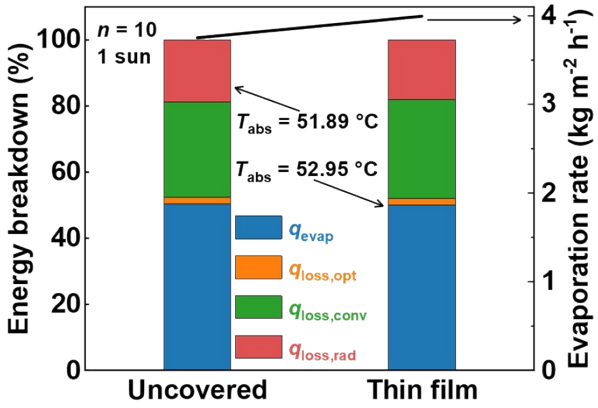


**Figure S17. The energy breakdown and evaporation rate of uncovered and thin film mode at *n* = 10 under 1 sun.**

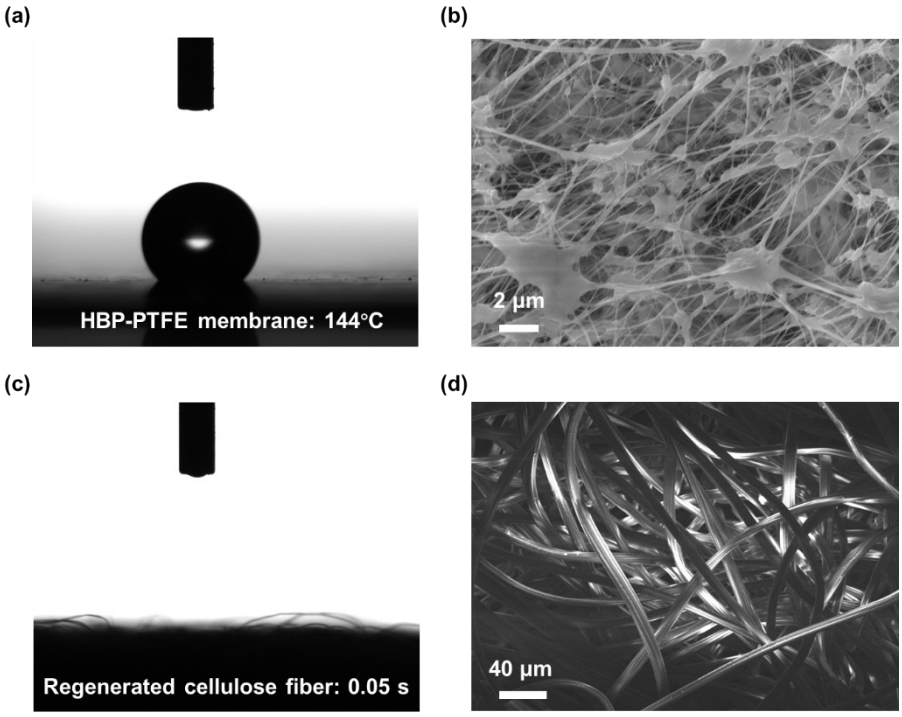


**Figure S18. The contact angle (a) and the SEM image (b) of the HBP-PTFE membrane. The contact angle (c) and the SEM image (d) of the regenerated cell fibers.**

### 5.4 Evaporation performance measurement

The diagram of the MSE device for measuring the evaporation performance is shown in Figure S19, including a photoradiometer, a data collector, a thermocouple, a solar simulator, a cover material, an MSE device, a fresh water collector, a balance, and a computer. The evaporation performance was tested under different operating conditions (e.g., various solar irradiation, from 1 sun to 3 suns) and designs (e.g., stages, from $n$ = 1 to $n$ = 10). The temperature and humidity of the test ambient were kept stable at about 23 °C and 60%, respectively. The incident intensity was provided by a solar simulator, with its power adjusted before each test to achieve different solar irradiation, and using a photoradiometer to calibrate prior to testing. For details on the construction of MSE devices at different stages and the operating principles of MSE devices, please refer to Section S5.3. Three materials (glass, acrylic, and aerogel) with

$3 \times 3 \times 1$ cm$^3$ in size were directly placed on top of the MSE device as the cover. The K-type thermocouples were connected to a multi-channel data collector and arranged at various positions on the MSE device (e.g., the upper surface of the cover, absorber layer, evaporation layer, condensation layer, etc.), to monitor temperature evolutions. A balance (accuracy 0.0001 g) was used to monitor the mass change of the fresh water collector, and the balance was connected to a computer to record the mass data in real-time. The mass measurement was started after the solar simulator was switched on, and the evaporation performance was calculated using the data after the MSE device had stabilized after the test was complete. We used the thin film case to represent the uncovered case and meanwhile enable water collection for experimentally comparing performances, for details of the film case diagram, see Section S5.3.

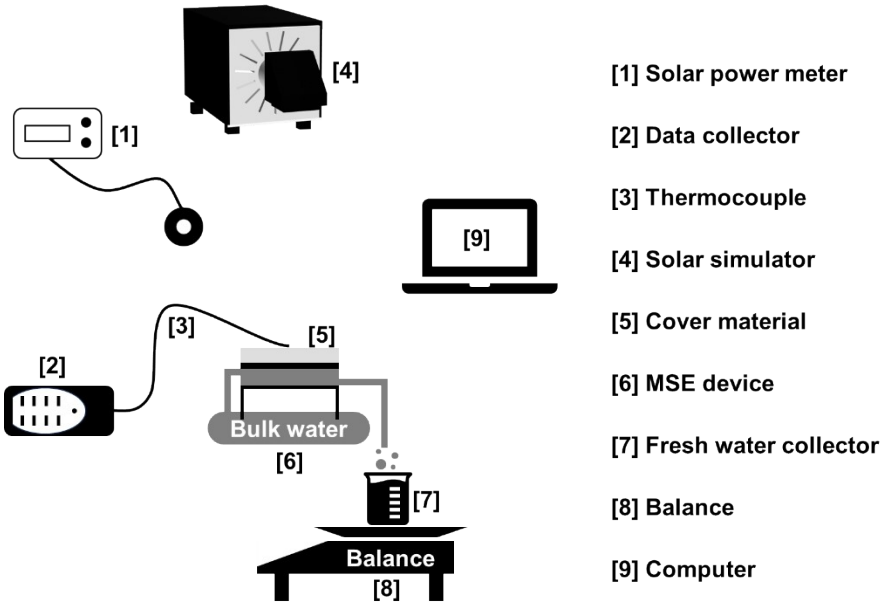


**Figure S19. The evaporation performance test schematic.**

The evaporation rate and evaporation efficiency were calculated by Eq. S26 and Eq. S27. The evaporation rate ($r_{evap,exp}$) is defined as the change in mass per unit area per unit time

$$r_{evap,exp} = \frac{\Delta m}{St} \tag{S26}$$

Where $\Delta m$ is the mass change, $S$ is the area of the evaporation region, and $t$ is the time

of the evaporation process. The evaporation efficiency ($\eta_{evap,exp}$) is defined as

$$\eta_{evap,exp} = \frac{m_w h_{lv}}{q_{sun}} \quad \text{(S27)}$$

where $m_w$ is the distillate yield, $h_{lv}$ is the amount of latent heat required of the water to change from the liquid to the vapor (2357 kJ kg$^{-1}$).

The experimental results of MSE devices operating under different operating conditions are shown in Figure S20 - S24.

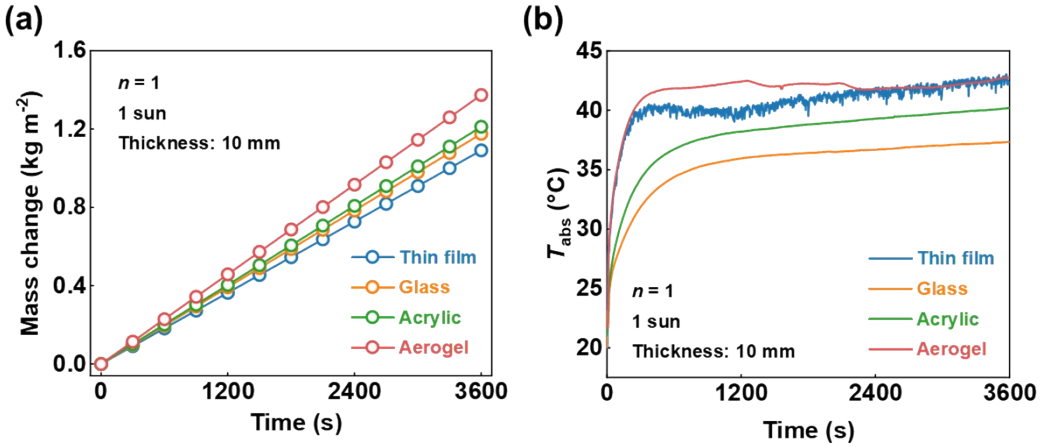


**Figure S20. The mass change and $T_{abs}$ as a function of time for MSE devices with a thin film, 10 mm thick glass, acrylic, and aerogel cover materials at $n$ = 1, 1 sun.**

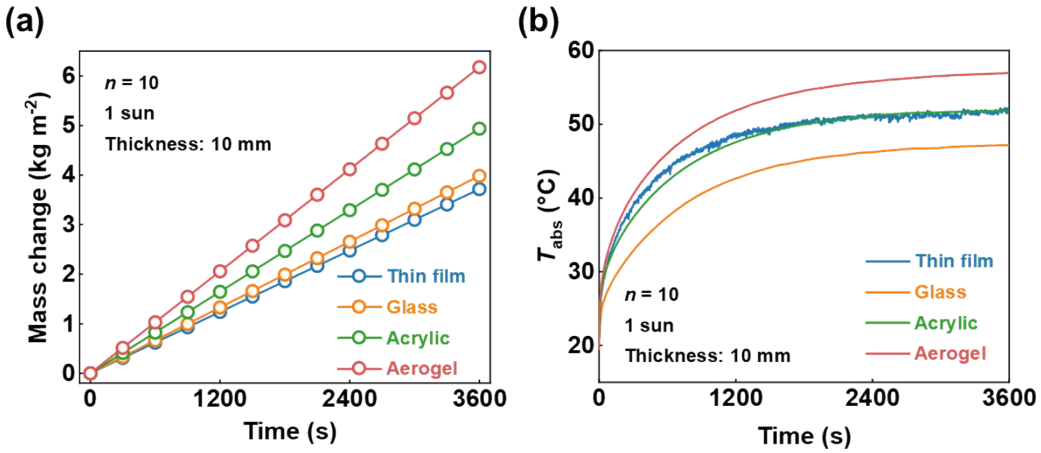


**Figure S21. The mass change and $T_{abs}$ as a function of time for MSE devices with**

**a thin film, 10 mm thick glass, acrylic, and aerogel cover materials at *n* = 10, 1 sun.**

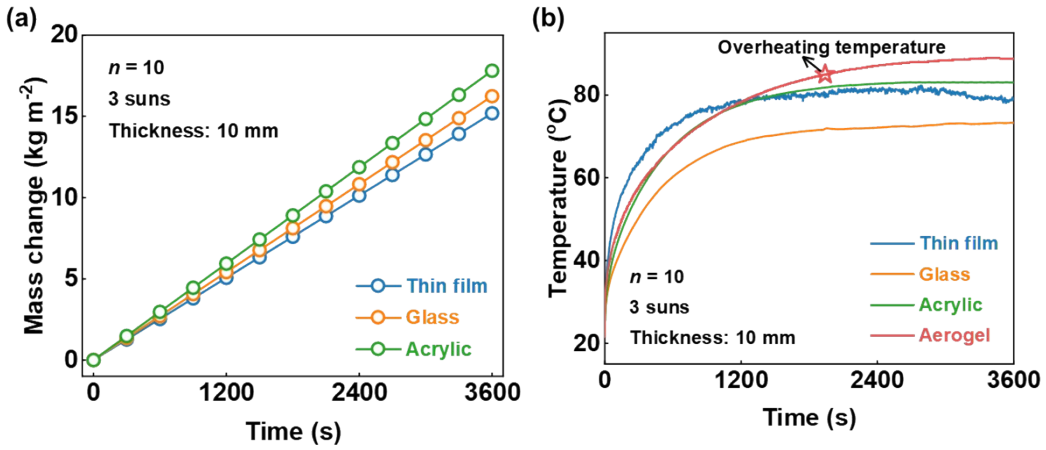


**Figure S22. The mass change and $T_{abs}$ as a function of time for MSE devices with a thin film, 10 mm thick glass, acrylic, and aerogel cover materials at *n* = 10, 3 suns.**

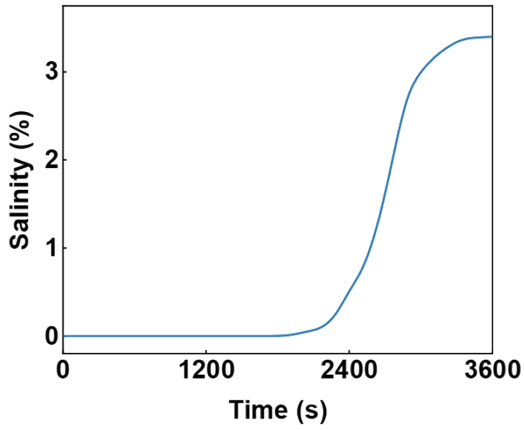


**Figure S23. The salinity as a function of time for MSE device with aerogel cover materials at *n* = 10, 3 suns.**

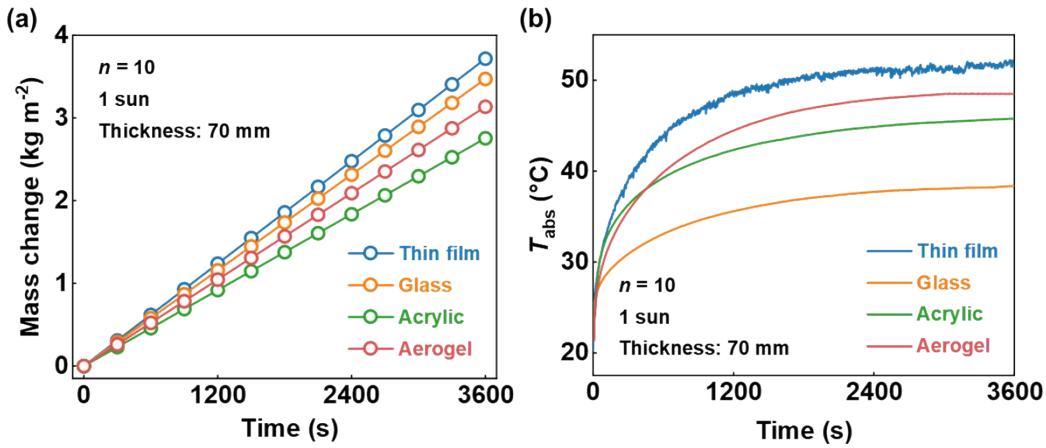


**Figure S24. The mass change and $T_{abs}$ as a function of time for MSE devices with a thin film, 70 mm thick glass, acrylic, and aerogel cover materials at $n$ = 10, 1 sun.**

### 5.5 Repeatability and durability of MSE device

We performed additional tests to verify the repeatability and durability of the MSE device ($n$ = 10, 1 sun, covered by 6 mm thick aerogel). We repeated the evaporation performance test for MSE twenty times (cycles). The same MSE device was used for all tests. After completing each test, the solar simulator was turned off, allowing the device to cool down before restarting the solar simulator for the subsequent repeatability test. Figure S25 shows that similar evaporation performances of the MSE device were achieved with a mass change of 6.18 ± 5% per hour after being used for 20 cycles with 3600 s irradiation under 1 sun condition for each cycle.

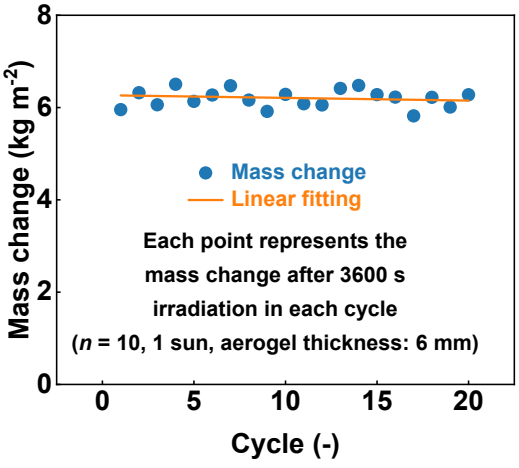

**Figure S25. Mass change of fresh water collected over 3600 s during different cycles with a 6 mm thick aerogel cover and $n$ = 10 under 1 sun irradiation.**

Meanwhile, the water contact angle, transmittance spectra of the aerogel sample, and absorption spectra of the absorber sample were explored after the 0th, 5th, 10th, 15th, and 20th cycles, and there was no obvious change after several cycles. The aerogel cover demonstrated excellent stability during the operation of the MSE device. The water contact angle remained within 140.5 ± 1.3% (see Figure S26), the transmittance spectrum was stable at 92.9 ± 0.2% (see Figure S27), and the absorption spectrum of the absorber stayed within 98.4 ± 0.2% (see Figure S28).

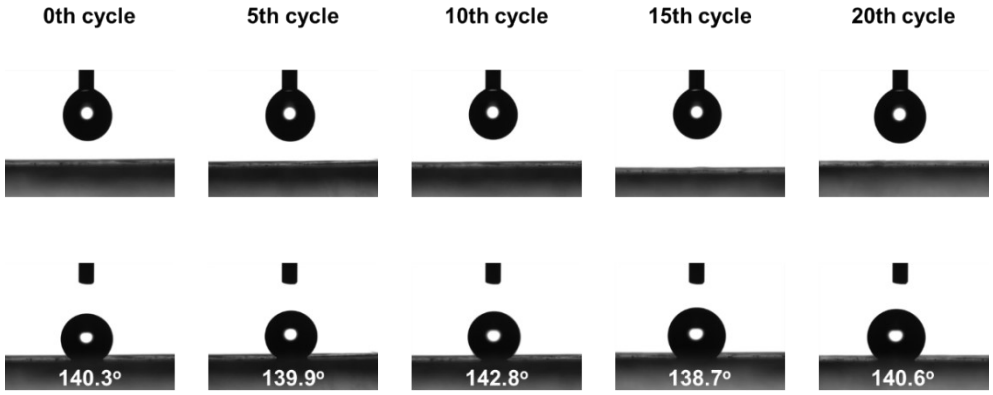


**Figure S26. The water contact angle of the aerogel after multiple evaporation experiment cycles.**

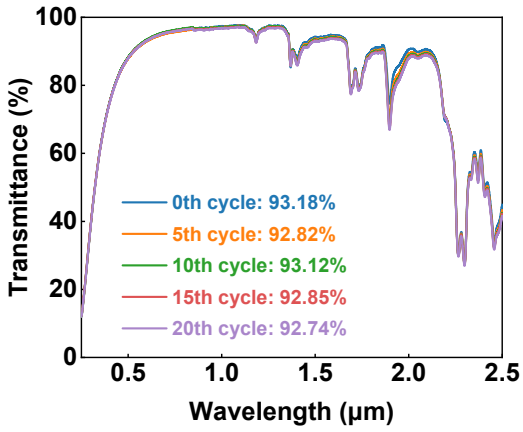


**Figure S27. Transmittance spectra of the aerogel in the solar band after multiple evaporation experiment cycles.**

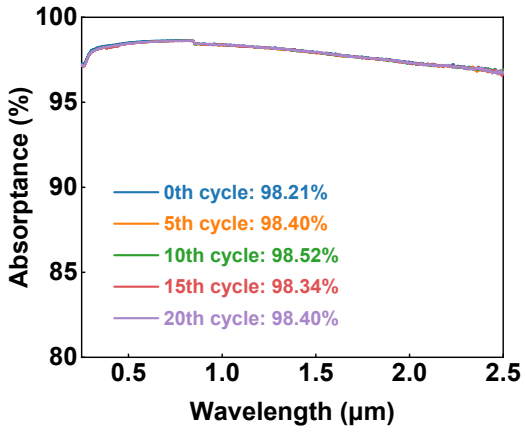


**Figure S28. Absorptance spectra of the absorber in the solar band after multiple evaporation experiment cycles.**

In addition, the durability of the MSE device can also be tested by the device operating stably under simulated seawater. To mitigate salt precipitation, an additional outlet has been designed in the evaporation layer (see Figure S29). Under 1 sun condition, the MSE device can be continuously operated in simulated seawater (i.e., 3.5% NaCl solution) for more than 20 h, at which time the evaporation rate is about 5.36 kg $m^{-2}$ $h^{-1}$ and the evaporation efficiency is about 357% (see Figure S30).

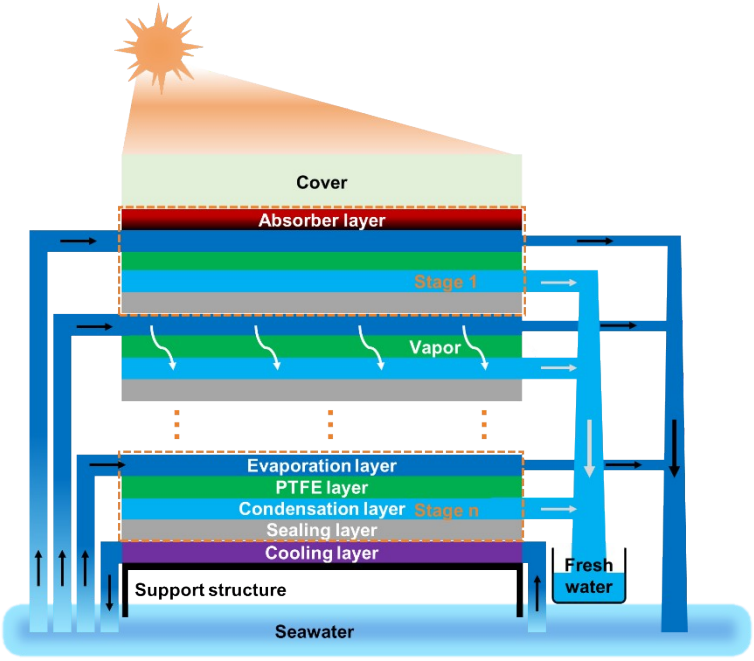


**Figure S29. The schematic diagram of the simulated seawater mode of the MSE device.**

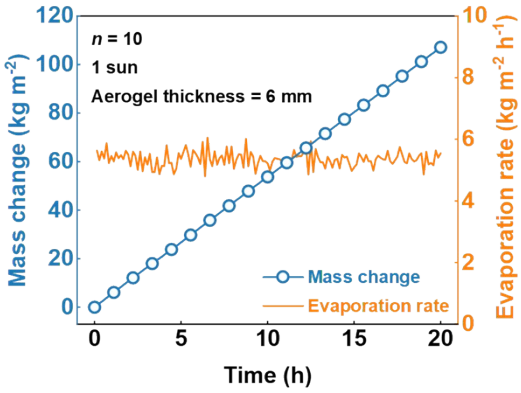


**Figure S30. The mass change and the corresponding evaporation rate of the MSE device with simulated seawater (continuous operation for 20 h at simulated seawater mode)**

**Section S6 – Economic analysis of MSE device**

Using a simple economic analysis, we evaluate the cost competitiveness of MSE devices with varying target cover materials and solar irradiations. The total cost of materials, manufacturing, labor, and maintenance represents the total cost of the device, as MSE devices rely solely on solar energy. The unit price for fresh water $P_w$ is thus given by[16],

$$P_w = \frac{C_m}{R_w \times C \times I_{irr} \times T_{life}} \tag{S28}$$

where $C_m$ is the total MSE device cost per unit area, $R_w$ is the fresh water productivity per unit area, C is the solar concentration, $I_{irr}$ is the average daily solar irradiation and $T_{life}$ is the MSE device lifetime. The MSE device contains cover materials, absorber, PE membrane, regenerated cell fibers, and PTFE membrane. Detailed information about the cost of materials is summarized in Table S3. Where the price of the aerogel material comes from Ref. [17], the absorber prices are estimated by PTFE membrane and nanocarbon powder, and other commercial material prices from Alibaba.com. To ensure consistency between water production rates and incident solar fluxes $R_w$ for MSE devices under varying operating conditions, a water production rate under 1 sun irradiation was used for calculations in this analysis. When the MSE device operates under high solar concentration, the corresponding water production rate at that concentration is used. However, the cost of the MSE device $C_w$ should also include adding a concentrator component. We use the average daily solar irradiation of China in our calculation (4.2 kWh $m^{-2}$ $day^{-1}$).

Table S3. Summary for MSE device unit cost (all unit costs correspond to MSE devices with single-stage).

| Component | Unit cost | Supplier |
|---|---|---|
| Glass | 11 \$ $m^{-2}$ | Jinan Jinbao Plastic Co., Ltd. |
| Acrylic | 15 \$ $m^{-2}$ | Lianyungang Huoyunquartz Technology Co., Ltd. |
| Aerogel | 40 \$ $m^{-2}$ | Ref. [17] |
| Absorber | 7.15 \$ $m^{-2}$ | Haining Chuangwei Filter Equipment Factory |
| PE membrane | 0.014 \$ $m^{-2}$ | Jinyang (Guangzhou) New Material Co., Ltd. |
| PTFE membrane | 7.13 \$ $m^{-2}$ | Haining Chuangwei Filter Equipment Factory |
| Regenerated cell fibers | 0.0884 \$ $m^{-2}$ | Dongyang Zhicheng Non-woven Co., Ltd. |
| Compound parabolic concentrator | 20 \$ $m^{-2}$ | Ref. [18] |

*Note that material prices data may vary slightly from country to country, however, these variations do not alter the conclusions we reached regarding the selection of the cover for the MSE device.

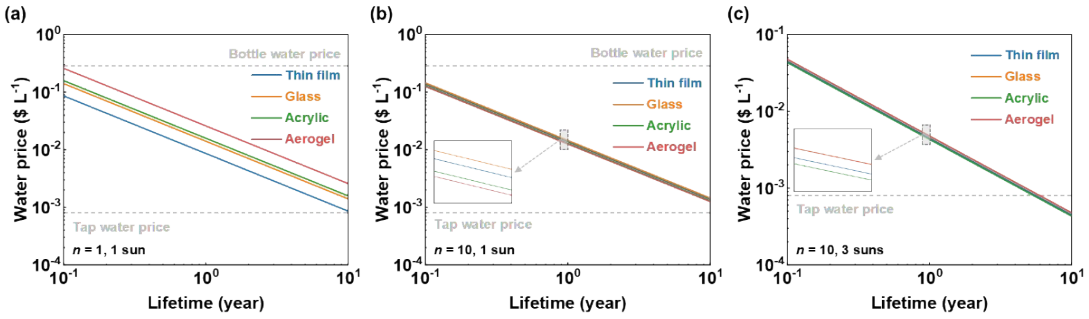


**Figure S31. Economic analysis for MSE devices with different cover materials. (a) *n* = 1, 1 sun. (b) *n* = 10, 1 sun. (c) *n* = 10, 3 suns.**

**Section S7 – Experimental instruments**

All the instruments used in the experiment are listed in Table S4.

**Table S4. Experimental instrument information.**

| Function | Equipment | Model | Manufacturer |
|---|---|---|---|
| Preparation | Magnetic stirrer | SN-MS-6D | Shanghai shangpu Instrument Equipment Co., Ltd. |
| | Ultrasonic Dispersion Machine | JY92-IIN | Ningbo Xinzhi Biotechnology Co., Ltd. |
| | Supercritical Dryer | SCD-350M | Tianjin Shianjia Biotechnology Co., Ltd. |
| | Drying cabinet | 101-1BS | Shanghai Li-Chen Instrument Technology Co., Ltd |
| | Box Furnace | KSL-1500X | Hefei Kejing Material Technology Co., Ltd |
| Characterization | Optical contact angle measuring instrument | Attention Theta Flex | Biolin Scientific Oy |
| | Inductively Coupled Plasma | Agilent 7700X | Agilent Technologies |

| | | | |
|---|---|---|---|
| | Mass Spectrometry (ICP-MS) | | (China) Co., Ltd |
| | Ultraviolet-Visible-Near Infrared Spectrophotometer | Lambda 750s | PerkinElmer |
| | Thermal Conductivity Instrument | Model TC300 | Xian XIATECH Technology Co., Ltd. |
| | Fourier Transform Infrared Spectrometer | Nicolet iS50 | Thermo Fisher Scientific (China) Co., Ltd. |
| | Scanning Electron Microscope (SEM) | Nova NanoSem450 | FEI |
| Process Monitor | Xenon Lamp Source | Microsolar300 | Beijing Perfectlight Technology Co. Ltd. |
| | Photoradiometer | PL-MW2000 | Beijing Perfectlight Technology Co., Ltd. |
| | Electronic Microbalance | ME | Mettler Toledo instruments (Shanghai) Co., Ltd |
| | 8 Channel Thermocouple | TC-08 | OMEGA Engineering |

**Section S8 – Summary of representative work in previous**

**Table S5. Review of demonstrators for solar evaporation.**

| No. | Year | Institute | Authors | Cover type | Stage | Solar intensity (kW $m^{-2}$) | Production rate (kg $m^{-2}$ $h^{-1}$) | Evaporation efficiency (%) | Water collection |
|---|---|---|---|---|---|---|---|---|---|
| 1 | 2018 | UT-Austin | Zhao et al.[19] | - | 1 | 1 | 3.2 | 94.0 | No |
| 2 | 2018 | UMD | Liu et al.[20] | - | 1 | 10 | 13.4 | 89.0 | No |
| 3 | 2017 | UMD | Jia et al.[21] | - | 1 | 10 | 13.0 | 86.7 | No |
| 4 | 2016 | NJU | Zhou et al.[22] | - | 1 | 4 | 1.4 | 90.0 | No |
| 5 | 2016 | MIT | Ni et al.[23] | - | 1 | 1 | 1.0 | 64.0 | No |
| 6 | 2016 | NJU | Li et al.[24] | - | 1 | 1 | 1.2 | 80.0 | No |
| 7 | 2015 | Tohoku U | Ito et al.[25] | - | 1 | 1 | 1.2 | 80.0 | No |
| 8 | 2015 | KAUST | Zhang et al.[26] | Glass cover | 1 | 1 | 0.9 | 58.0 | Yes |
| 9 | 2015 | Yonsei U | Bae et al.[27] | - | 1 | 20 | 17.1 | 57.0 | No |
| 10 | 2010 | Anno U | Sakthivel et al.[28] | Glass cover | 1 | Outdoor | 0.8 | 52.0 | Yes |

| | | | | | | | | | |
|---|---|---|---|---|---|---|---|---|---|
| 11 | 2021 | SJTU | Shi et al.[29] | - | 1 | 1 | 1.2 | 82.0 | No |
| 12 | 2009 | Tanta U | Kabeel[30] | Glass cover | 1 | 1 | 0.7 | 45.0 | Yes |
| 13 | 2008 | IJCE | Velmurugan et al.[31] | Glass cover | 1 | Outdoor | 0.3 | 21.8 | Yes |
| 14 | 2020 | SCU | Yang et al.[32] | Glass cover | 1 | 8 | 5.8 | 48.3 | Yes |
| 15 | 2022 | NFU | Lu et al.[33] | - | 1 | 1 | 2.7 | 86.0 | No |
| 16 | 2024 | SDFMU | Ding et al.[34] | Glass cover | 1 | 1 | 3.1 | 209.3 | Yes |
| 17 | 2020 | NJU | Li et al.[35] | - | 1 | 1 | 10.9 | 741.5 | No |
| 18 | 2019 | SDFMU | Li et al.[36] | - | 1 | 1 | 2.1 | 91.5 | No |
| 19 | 2018 | UMD | Li et al.[37] | - | 1 | 1 | 1.2 | 80.0 | No |
| 19a | 2018 | UMD | Li et al.[37] | - | 1 | 10 | 1.3 | 89.0 | No |
| 20 | 2019 | CUMT | Liu et al.[38] | - | 1 | 1 | 1.3 | 91.5 | No |
| 21 | 2018 | MIT | Ni et al.[39] | Polymer-film | 1 | 1 | 0.9 | 59.5 | Yes |
| 22 | 2017 | FDU | Liu et al.[40] | - | 1 | 1 | 1.3 | 88.0 | No |
| 23 | 2022 | MIT | Zhang et al.[41] | - | 1 | 1 | 1.2 | 85.0 | No |
| 24 | 2017 | NJU | Xu et al.[42] | - | 1 | 1 | 1.1 | 78.0 | No |
| 25 | 2019 | NJU | Xu et al.[43] | - | 1 | 1 | 1.2 | 80.0 | No |

| | | | | | | | | | |
|---|---|---|---|---|---|---|---|---|---|
| 26 | 2022 | KAUST | Yang et al.[44] | PMMA cover | 1 | Outdoor | 0.6 | 40.0 | Yes |
| 27 | 2015 | SJTU | Liu et al.[45] | - | 1 | 4.5 | 1.1 | 77.8 | No |
| 28 | 2017 | PolyU | Ma et al.[46] | - | 1 | 3 | 0.8 | 55.0 | No |
| 29 | 2016 | CAS | Zhu et al.[47] | - | 1 | 1 | 1.0 | 70.9 | No |
| 30 | 2017 | UMD | Chen et al.[48] | - | 1 | 10 | 1.2 | 81.0 | No |
| 31 | 2017 | HIT | Wang et al.[49] | - | 1 | 10 | 1.2 | 85.0 | No |
| 32 | 2017 | WUSL | Liu et al.[50] | - | 1 | 12 | 1.2 | 83.0 | No |
| 33 | 2017 | HIT | Wang et al.[51] | - | 1 | 5 | 3.6 | 40.0 | No |
| 34 | 2017 | HUBU | Wang et al.[52] | - | 1 | 1 | 0.9 | 60.0 | No |
| 34a | 2017 | HUBU | Wang et al.[52] | - | 1 | 4 | 1.1 | 74.8 | No |
| 35 | 2017 | HUST | Xue et al.[53] | - | 1 | 1 | 1.1 | 72.0 | No |
| 36 | 2013 | Rice | Neumann et al.[54] | - | 1 | 1 | 1.2 | 80.0 | No |
| 37 | 2021 | CSU | Yin et al.[55] | - | 1 | 1 | 7.6 | 506.7 | No |
| 38 | 2022 | Tongji | Wang et al.[56] | - | 1 | 1 | 11.6 | 772.0 | No |
| 39 | 2023 | DHU | Liu et al.[57] | - | 1 | 1 | 8.3 | 554.0 | No |
| 40 | 2016 | NJU | Zhou et al.[58] | - | 1 | 4 | 5.4 | 90.0 | No |

| | | | | | | | | | |
|---|---|---|---|---|---|---|---|---|---|
| 41 | 2018 | NJU | Li et al.[59] | - | 1 | 1 | 1.6 | 110.2 | No |
| 42 | 2023 | ZJU | Cheng et al.[60] | Quartz glass | 7 | 1 | 2.2 | 149.7 | Yes |
| 42a | 2023 | ZJU | Cheng et al.[60] | Quartz glass | 7 | 2 | 4.8 | 163.3 | Yes |
| 43 | 2021 | KAUST | Wang et al.[61] | Solar cell | 5 | 1 | 2.5 | 166.7 | Yes |
| 44 | 2020 | WHU | Jiang et al.[62] | Aluminum plate | 4 | 1 | 1.4 | 96.6 | Yes |
| 45 | 2019 | KAUST | Wang et al.[63] | Photovoltaic panel | 5 | 1 | 3.3 | 221.1 | Yes |
| 46 | 2021 | KAUST | Wang et al.[64] | EVA film | 8 | 1 | 3.6 | 245.6 | Yes |
| 47 | 2023 | SJTU | Xu et al.[65] | Glass cover | 3 | 1 | 2.1 | 144.2 | Yes |
| 48 | 2020 | SJTU / MIT | Xu et al.[17] | Silica aerogel | 10 | 1 | 5.8 | 385.0 | Yes |
| 49 | 2021 | UJN | Yang et al.[66] | Photovoltaic | 5 | 1 | 1.2 | 79.6 | Yes |
| 50 | 2023 | BIT | Zhu et al.[67] | Glass cover | 10 | 1 | 5.2 | 354.0 | Yes |
| 51 | 2024 | BIT | Zhu et al.[68] | Glass cover | 1 | 1 | 1.0 | 68.8 | Yes |
| 52 | 2022 | SJTU | Han et al.[69] | Glass cover | 1 | 1 | 0.8 | 51.1 | Yes |
| 53 | 2023 | HIT | Liu et al.[70] | Polyethylene | 10 | 1 | 5.4 | 358.0 | Yes |

| | | | | | | | | | |
|---|---|---|---|---|---|---|---|---|---|
| | | | | resin | | | | | |
| 54 | 2024 | CityU | Mao et al.[71] | Heat sink | 1 | 1 | 2.8 | 191.2 | Yes |
| 55 | 2023 | SJTU | Gao et al.[72] | Glass cover | 10 | 1 | 4.7 | 322.0 | Yes |
| 56 | 2018 | HUST | Xue et al.[73] | Bubble wrap | 2 | 1 | 1.0 | 72.0 | Yes |
| 57 | 2018 | POLITO | Chiavazzo et al.[74] | Polyethylene | 10 | 0.9 | 3.0 | 226.8 | Yes |
| 58 | 2023 | DHU | Gao et al.[75] | Janus fabric | 1 | 1 | 1.2 | 78.0 | Yes |
| 59 | 2021 | NJU | Wang et al.[76] | Olydimethylsiloxane film | 1 | 1 | 1.1 | 70.0 | Yes |
| 60 | 2020 | POLITO / MIT | Morciano et al.[77] | Polyethylene | 3 | 0.95 | 2.0 | 163.2 | Yes |
| 61 | 2024 | DHU | Tian et al.[78] | Copper plate | 8 | 1 | 2.3 | 153.1 | Yes |

**References**


[1] Al Shehri A, Parrott B, Carrasco P, et al. Impact of dust deposition and brush-based dry cleaning on glass transmittance for PV modules applications. *Solar Energy*, **2016**, 135: 317-324.

[2] Giovannetti F, Föste S, Ehrmann N, et al. High transmittance, low emissivity glass covers for flat plate collectors: Applications and performance. *Solar energy*, **2014**, 104: 52-59.

[3] Jia C, Chen C, Mi R, et al. Clear wood toward high-performance building materials. *ACS nano*, **2019**, 13(9): 9993-10001.

[4] Jiandong Z, Hanzhong T, Susu C. Numerical simulation for structural parameters of flat-plate solar collector. *Solar Energy*, **2015**, 117: 192-202.

[5] Maduru V R, Shaik S, Cuce E, et al. UV coated acrylics as a substitute for generic glazing in buildings of Indian climatic conditions: Prospective for energy savings, CO2 abatement, and visual acceptability. *Energy and Buildings*, **2022**, 268: 112231.

[6] Murtadha T K. Installing clear acrylic sheet to reduce unwanted sunlight waves that photovoltaic panels receive. *Results in Engineering*, **2023**, 17: 100875.

[7] Ming Y, Sun Y, Liu X, et al. Optical evaluation of a smart transparent insulation material for window application. *Energy Conversion and Management: X*, **2022**, 16: 100315.

[8] Zhao L, Bhatia B, Yang S, et al. Harnessing heat beyond 200 C from unconcentrated sunlight with nonevacuated transparent aerogels. *ACS nano*, **2019**, 13(7): 7508-7516.

[9] Reim M, Reichenauer G, Körner W, et al. Silica-aerogel granulate–Structural, optical and thermal properties. *Journal of non-crystalline solids*, **2004**, 350: 358-363.

[10] Günay A A, Kim H, Nagarajan N, et al. Optically transparent thermally insulating silica aerogels for solar thermal insulation. *ACS applied materials & interfaces*, **2018**, 10(15): 12603-12611.

[11] Li X, Yang Z, Li K, et al. A flexible silica aerogel with good thermal and acoustic insulation prepared via water solvent system. *Journal of Sol-Gel Science and Technology*, **2019**, 92: 652-661.

[12] Jensen K I. Passive solar component based on evacuated monolithic silica aerogel. *Journal of non-crystalline solids*, **1992**, 145: 237-239.

[13] Liu H, Li Z Y, Zhao X P, et al. Study on unit cell models and the effective thermal conductivities of silica aerogel. *Journal of nanoscience and nanotechnology*, **2015**, 15(4): 3218-3223.

[14] Li Z Y, Liu H, Zhao X P, et al. A multi-level fractal model for the effective thermal conductivity of silica aerogel. *Journal of Non-Crystalline Solids*, **2015**, 430: 43-51.

[15] Liu H, Zhao X. Thermal conductivity analysis of high porosity structures with open and closed pores. *International Journal of Heat and Mass Transfer*, **2022**, 183: 122089.

[16] Zhang L, Xu Z, Zhao L, et al. Passive, high-efficiency thermally-localized solar desalination. *Energy & Environment Science*, **2021**, 14(4): 1771-1793.

[17] Xu Z, Zhang L, Zhao L, et al. Ultrahigh-efficiency desalination via a thermally-localized multistage solar still. *Energy & Environmental Science*, **2020**, 13(3): 830-839.

[18] Zhao L, Bhatia B, Zhang L, et al. A passive high-temperature high-pressure solar steam generator for medical sterilization. *Joule*, **2020**, 4(12): 2733-2745.

[19] Zhao F, Zhou X, Shi Y, et al. Highly efficient solar vapour generation via hierarchically nanostructured gels. *Nature nanotechnology*, **2018**, 13(6): 489-495.

[20] Liu H, Chen C, Chen G, et al. High-performance solar steam device with layered channels: artificial tree with a reversed design. *Advanced Energy Materials*, **2018**, 8(8): 1701616.

[21] Jia C, Li Y, Yang Z, et al. Rich mesostructures derived from natural woods for solar steam generation. *Joule*, **2017**, 1(3): 588-599.

[22] Zhou L, Tan Y, Ji D, et al. Self-assembly of highly efficient, broadband plasmonic absorbers for solar steam generation. *Science advances*, **2016**, 2(4): e1501227.

[23] Ni G, Li G, Boriskina S V, et al. Steam generation under one sun enabled by a floating structure with thermal concentration. *Nature Energy*, **2016**, 1(9): 1-7.

[24] Li X, Xu W, Tang M, et al. Graphene oxide-based efficient and scalable solar desalination under one sun with a confined 2D water path. *Proceedings of the National*

*Academy of Sciences*, **2016**, 113(49): 13953-13958.

[25] Ito Y, Tanabe Y, Han J, et al. Multifunctional Porous Graphene for High-Efficiency Steam Generation by Heat Localization. *Advanced materials*, **2015**, 27(29): 4302-4307.

[26] Zhang L, Tang B, Wu J, et al. Hydrophobic light-to-heat conversion membranes with self-healing ability for interfacial solar heating. *Advanced materials*, **2015**, 27(29): 4889-4894.

[27] Bae K, Kang G, Cho S K, et al. Flexible thin-film black gold membranes with ultrabroadband plasmonic nanofocusing for efficient solar vapour generation. *Nature communications*, **2015**, 6(1): 10103.

[28] Sakthivel M, Shanmugasundaram S, Alwarsamy T. An experimental study on a regenerative solar still with energy storage medium—Jute cloth. *Desalination*, **2010**, 264(1-2): 24-31.

[29] Shi J, Luo X, Liu Z, et al. Efficient and antifouling interfacial solar desalination guided by a transient salt capacitance model. *Cell Reports Physical Science*, **2021**, 2(2): 1-14.

[30] Kabeel A E. Performance of solar still with a concave wick evaporation surface. *Energy*, **2009**, 34(10): 1504-1509.

[31] Velmurugan V, Gopalakrishnan M, Raghu R, et al. Single basin solar still with fin for enhancing productivity. *Energy Conversion and Management*, **2008**, 49(10): 2602-2608.

[32] Yang H, Sun Y, Peng M, et al. Tailoring the salt transport flux of solar evaporators for a highly effective salt-resistant desalination with high productivity. *ACS nano*, **2022**, 16(2): 2511-2520.

[33] Lu Y, Fan D, Shen Z, et al. Design and performance boost of a MOF-functionalized-wood solar evaporator through tuning the hydrogen-bonding interactions. *Nano Energy*, **2022**, 95: 107016.

[34] Ding M, Zhao D, Feng P, et al. Highly efficient three‐dimensional solar evaporator for zero liquid discharge desalination of high‐salinity brine. *Carbon*

*Energy*, **2024**: e548.

[35] Li J, Wang X, Lin Z, et al. Over 10 kg $m^{-2}$ $h^{-1}$ evaporation rate enabled by a 3D interconnected porous carbon foam. *Joule*, **2020**, 4(4): 928-937.

[36] Li W, Li Z, Bertelsmann K, et al. Portable low-pressure solar steaming-collection unisystem with polypyrrole origamis. *Advanced Materials*, **2019**, 31(29): 1900720.

[37] Li T, Liu H, Zhao X, et al. Scalable and highly efficient mesoporous wood‐based solar steam generation device: localized heat, rapid water transport. *Advanced Functional Materials*, **2018**, 28(16): 1707134.

[38] Liu S, Huang C, Huang Q, et al. A new carbon-black/cellulose-sponge system with water supplied by injection for enhancing solar vapor generation. *Journal of materials chemistry A*, **2019**, 7(30): 17954-17965.

[39] Ni G, Zandavi S H, Javid S M, et al. A salt-rejecting floating solar still for low-cost desalination. *Energy & Environmental Science*, **2018**, 11(6): 1510-1519.

[40] Liu Z, Song H, Ji D, et al. Extremely cost‐effective and efficient solar vapor generation under nonconcentrated illumination using thermally isolated black paper. *Global Challenges*, **2017**, 1(2): 1600003.

[41] Zhang L, Li X, Zhong Y, et al. Highly efficient and salt rejecting solar evaporation via a wick-free confined water layer. *Nature Communications*, **2022**, 13(1): 849.

[42] Xu N, Hu X, Xu W, et al. Mushrooms as efficient solar steam‐generation devices. *Advanced Materials*, **2017**, 29(28): 1606762.

[43] Xu N, Li J, Wang Y, et al. A water lily–inspired hierarchical design for stable and efficient solar evaporation of high-salinity brine. *Science advances*, **2019**, 5(7): 7013.

[44] Yang K, Pan T, Dang S, et al. Three-dimensional open architecture enabling salt-rejection solar evaporators with boosted water production efficiency. *Nature Communications*, **2022**, 13(1): 6653.

[45] Liu Y, Yu S, Feng R, et al. A bioinspired, reusable, paper‐based system for high‐performance large‐scale evaporation. *Advanced Materials*, **2015**, 27(17): 2768-2774.

[46] Ma S, Chiu C P, Zhu Y, et al. Recycled waste black polyurethane sponges for solar vapor generation and distillation. *Applied energy*, **2017**, 206: 63-69.

[47] Zhu G, Xu J, Zhao W, et al. Constructing black titania with unique nanocage structure for solar desalination. *ACS applied materials & interfaces*, **2016**, 8(46): 31716-31721.

[48] Chen C, Li Y, Song J, et al. Highly flexible and efficient solar steam generation device. *Advanced materials*, **2017**, 29(30): 1701756.

[49] Wang X, He Y, Liu X, et al. Solar steam generation through bio-inspired interface heating of broadband-absorbing plasmonic membranes. *Applied Energy*, **2017**, 195: 414-425.

[50] Liu K K, Jiang Q, Tadepalli S, et al. Wood–graphene oxide composite for highly efficient solar steam generation and desalination. *ACS applied materials & interfaces*, **2017**, 9(8): 7675-7681.

[51] Wang X, He Y, Liu X, et al. Enhanced direct steam generation via a bio-inspired solar heating method using carbon nanotube films. *Powder technology*, **2017**, 321: 276-285.

[52] Wang G, Fu Y, Ma X, et al. Reusable reduced graphene oxide based double-layer system modified by polyethylenimine for solar steam generation. *Carbon*, **2017**, 114: 117-124.

[53] Xue G, Liu K, Chen Q, et al. Robust and low-cost flame-treated wood for high-performance solar steam generation. *ACS applied materials & interfaces*, **2017**, 9(17): 15052-15057.

[54] Neumann O, Urban A S, Day J, et al. Solar vapor generation enabled by nanoparticles. *ACS nano*, **2013**, 7(1): 42-49.

[55] Yin K, Wu Z, Wu J, et al. Solar-driven thermal-wind synergistic effect on laser-textured superhydrophilic copper foam architectures for ultrahigh efficient vapor generation. *Applied Physics Letters*, **2021**, 118(21): 211905.

[56] Wang H, Zhang C, Ji X, et al. Over 11 kg $m^{-2}$ $h^{-1}$ Evaporation Rate Achieved by Cooling Metal–Organic Framework Foam with Pine Needle-Like Hierarchical

Structures to Subambient Temperature. *ACS Applied Materials & Interfaces*, **2022**, 14(8): 10257-10266.

[57] Liu Y, Luo B, Liu H, et al. 3D printed electrospun nanofiber-based pyramid-shaped solar vapor generator with hierarchical porous structure for efficient desalination. *Chemical Engineering Journal*, **2023**, 452: 139402.

[58] Zhou L, Tan Y, Ji D, et al. Self-assembly of highly efficient, broadband plasmonic absorbers for solar steam generation. *Science advances*, **2016**, 2(4): e1501227.

[59] Li X, Li J, Lu J, et al. Enhancement of interfacial solar vapor generation by environmental energy. *Joule*, **2018**, 2(7): 1331-1338.

[60] Cheng S, Li Y, Jin B, et al. A stable all-day interfacial evaporation multistage distillation driven by solar photothermal and solar electrothermal. *Solar Energy*, **2023**, 264: 112065.

[61] Wang W, Aleid S, Shi Y, et al. Integrated solar-driven PV cooling and seawater desalination with zero liquid discharge. *Joule*, **2021**, 5(7): 1873-1887.

[62] Huang L, Wang Y, He R, et al. Solar-driven co-generation of electricity and water by evaporation cooling. *Desalination*, **2020**, 488: 114533.

[63] Wang W, Shi Y, Zhang C, et al. Simultaneous production of fresh water and electricity via multistage solar photovoltaic membrane distillation. *Nature communications*, **2019**, 10(1): 3012.

[64] Wang W, Shi Y, Zhang C, et al. Solar seawater distillation by flexible and fully passive multistage membrane distillation. *Nano Letters*, **2021**, 21(12): 5068-5074.

[65] Xu Z, Yu J, Shan H, et al. Solar evaporation with solute replacement towards real-world applications. *Energy & Environmental Science*, **2023**, 16(11): 5325-5338.

[66] Yang L, Sun T, Tang J, et al. Photovoltaic-multistage desalination of hypersaline waters for simultaneous electricity, water and salt harvesting via automatic rinsing. *Nano Energy*, **2021**, 87: 106163.

[67] Zhu Z, Zheng H, Kong H, et al. Passive solar desalination towards high efficiency and salt rejection via a reverse-evaporating water layer of millimetre-scale thickness. *Nature Water*, **2023**, 1(9): 790-799.

[68] Zhu Z, Zheng H, Liu Z, et al. Understanding the effect of the condensation temperature on solar-driven reverse distillation for enhanced water production. *Energy Conversion and Management*, 2024, 301: 118024.

[69] Han W, Gao J, Yu J, et al. Efficient and low-cost solar desalination device with enhanced condensation on nail arrays. *Desalination*, **2022**, 544: 116132.

[70] Liu S, Li S, Lin M. Understanding interfacial properties for enhanced solar evaporation devices: From geometrical to physical interfaces. *ACS Energy Letters*, **2023**, 8(4): 1680-1687.

[71] Mao Z, Yao Y, Shen J, et al. Passive interfacial cooling-induced sustainable electricity–water cogeneration. *Nature Water*, **2024**: 1-8.

[72] Gao J, Zhang L, You J, et al. Extreme salt-resisting multistage solar distillation with thermohaline convection. *Joule*, **2023**, 7(10): 2274-2290.

[73] Xue G, Chen Q, Lin S, et al. Highly efficient water harvesting with optimized solar thermal membrane distillation device. *Global Challenges*, **2018**, 2(5-6): 1800001.

[74] Chiavazzo E, Morciano M, Viglino F, et al. Passive solar high-yield seawater desalination by modular and low-cost distillation. *Nature sustainability*, **2018**, 1(12): 763-772.

[75] Gao C, Zhou B, Li J, et al. Reversed vapor generation with Janus fabric evaporator and comprehensive thermal management for efficient interfacial solar distillation. *Chemical Engineering Journal*, **2023**, 463: 142002.

[76] Wang F, Xu N, Zhao W, et al. A high-performing single-stage invert-structured solar water purifier through enhanced absorption and condensation. *Joule*, **2021**, 5(6): 1602-1612.

[77] Morciano M, Fasano M, Boriskina S V, et al. Solar passive distiller with high productivity and Marangoni effect-driven salt rejection. *Energy & Environmental Science*, **2020**, 13(10): 3646-3655.

[78] Tian Y, Jiang Y, Zhu R, et al. Solar-Driven Multistage Device Integrating Dropwise Condensation and Guided Water Transport for Efficient Freshwater and Salt Collection. *Environmental Science & Technology*, **2024**, 58(17): 7335-7345.